

Next-Generation Parametric Reduced-Order Models

Sung-Kwon Hong^a, Bogdan I. Epureanu^{a,*},
Matthew P. Castanier^b

*^aDepartment of Mechanical Engineering, University of Michigan
2350 Hayward Street, Ann Arbor, Michigan 48109-2125, USA*

*^bU.S. Army Tank Automotive Research, Development, and Engineering Center
Warren, MI 48397-5000, USA*

Abstract

Novel parametric reduced-order models are proposed for fast reanalysis to predict the dynamic response of complex structures, which suffered thickness variations caused by design changes or damage in one or more substructures. Parametric reduced-order models developed previously have two important challenges to overcome to improve accuracy and performance: (a) the transformation matrix is not mathematically stable, (b) the Taylor series parameterization techniques do not capture thickness variations of the structure modeled with solid-type elements due to the highly nonlinear dependence on thickness changes. Thus, herein, a new transformation matrix and novel parameterization techniques are proposed. Usual reduced-order models have an additional challenge, namely the difficulty in reducing the interface degrees of freedom. Thus a way of reducing the interface degrees of freedom is also proposed. The predicted vibration responses of complex structures are shown to agree very well with results obtained using a much

*Corresponding author. Tel.: +1-734-647-6391; fax: +1-734-764-4256

Email addresses: sungkwon@umich.edu (Sung-Kwon Hong),
epureanu@umich.edu (Bogdan I. Epureanu), matt.castanier@us.army.mil (Matthew P. Castanier)

Report Documentation Page

Form Approved
OMB No. 0704-0188

Public reporting burden for the collection of information is estimated to average 1 hour per response, including the time for reviewing instructions, searching existing data sources, gathering and maintaining the data needed, and completing and reviewing the collection of information. Send comments regarding this burden estimate or any other aspect of this collection of information, including suggestions for reducing this burden, to Washington Headquarters Services, Directorate for Information Operations and Reports, 1215 Jefferson Davis Highway, Suite 1204, Arlington VA 22202-4302. Respondents should be aware that notwithstanding any other provision of law, no person shall be subject to a penalty for failing to comply with a collection of information if it does not display a currently valid OMB control number.

1. REPORT DATE 03 NOV 2011			2. REPORT TYPE Journal Article			3. DATES COVERED 03-11-2011 to 03-11-2011		
4. TITLE AND SUBTITLE NEXT-GENERATION PARAMETRIC REDUCED-ORDER MODELS						5a. CONTRACT NUMBER w56h2v-04-2-0001		
						5b. GRANT NUMBER		
						5c. PROGRAM ELEMENT NUMBER		
6. AUTHOR(S) Matt Castanier; Sung-Kwon Hong; Bogdan Epureanu						5d. PROJECT NUMBER		
						5e. TASK NUMBER		
						5f. WORK UNIT NUMBER		
7. PERFORMING ORGANIZATION NAME(S) AND ADDRESS(ES) U.S. Army TARDEC ,6501 E.11 Mile Rd,Warren,MI,48397-5000						8. PERFORMING ORGANIZATION REPORT NUMBER #22384		
9. SPONSORING/MONITORING AGENCY NAME(S) AND ADDRESS(ES) U.S. Army TARDEC, 6501 E.11 Mile Rd, Warren, MI, 48397-5000						10. SPONSOR/MONITOR'S ACRONYM(S) TARDEC		
						11. SPONSOR/MONITOR'S REPORT NUMBER(S) #22384		
12. DISTRIBUTION/AVAILABILITY STATEMENT Approved for public release; distribution unlimited								
13. SUPPLEMENTARY NOTES								
14. ABSTRACT Novel parametric reduced-order models are proposed for fast reanalysis to predict the dynamic response of complex structures, which suffered thickness variations caused by design changes or damage in one or more substructures. Parametric reduced-order models developed previously have two important challenges to overcome to improve accuracy and performance: (a) the transformation matrix is not mathematically stable, (b) the Taylor series parameterization techniques do not capture thickness variations of the structure modeled with solid-type elements due to the highly nonlinear dependence on thickness changes. Thus, herein, a new transformation matrix and novel parameterization techniques are proposed. Usual reduced-order models have an additional challenge, namely the difficulty in reducing the interface degrees of freedom. Thus a way of reducing the interface degrees of freedom is also proposed. The predicted vibration responses of complex structures are shown to agree very well with results obtained using a much more computationally expensive commercial tool.								
15. SUBJECT TERMS parametric reduced order models, thickness variation, transformation matrix, parameterization techniques, interface reduction								
16. SECURITY CLASSIFICATION OF:						17. LIMITATION OF ABSTRACT	18. NUMBER OF PAGES	19a. NAME OF RESPONSIBLE PERSON
a. REPORT unclassified		b. ABSTRACT unclassified		c. THIS PAGE unclassified		Same as Report (SAR)	55	

more computationally expensive commercial tool.

Keywords: parametric reduced order models, thickness variation, transformation matrix, parameterization techniques, interface reduction

1. Introduction

Component mode synthesis techniques are well established [1, 2, 3, 4, 5, 6, 7] in the field of structural dynamic analysis as an alternative to conventional finite element models (FEMs) with large number of degrees of freedom (DOFs). Component mode synthesis (CMS) belongs to a wide class of domain decomposition techniques. CMS is a substructural based technique, which divides the global structure into several substructures, and the DOFs of those substructures are reduced significantly. Then, each individual substructure in the CMS domain is reconnected, and the system dynamic responses are predicted very efficiently and accurately.

CMS has become a very popular numerical tool in aerospace and automotive engineering because it usually meets high standards of computational efficiency. Computational efficiency is illustrated by significant cost saving when remeshing is needed, since this task can be done locally, i.e. on each substructure separately. However, the remeshing process might also be time consuming computationally and manually for design purposes such as structural optimization, and for damage modeling for structural health monitoring. Therefore, reduced-order modeling techniques for design and damage modeling purposes are needed.

The reduced-order models (ROMs) for design and damage modeling were introduced almost fifteen years ago by Balmés et al. [8, 9] to avoid the relatively expensive process of reanalysis of complex structures. In addition, several other

ROMs referred to as parametric reduced-order models (PROMs) have been developed [10, 11, 12, 13]. In particular, multi-component PROMs (MC-PROMs) have been developed recently by Hong et al. [13]. For robust substructure (re)analysis, MC-PROMs are advantageous because they allow several substructures to have parametric variability in characteristics such as geometric parameters (e.g., thickness), or material properties (e.g., Young's modulus). MC-PROMs are perfectly suited for predicting the vibration response of structures modeled with shell-type finite elements which can have thickness variations. However, if the structure is modeled with brick-type finite elements, and if the brick-type elements require local volume changes during reanalysis, then MC-PROMs cannot be effectively used to predict the dynamic response. This is because MC-PROMs use third-order Taylor series for parameterization. These Taylor series do not capture accurately the variation of the mass and stiffness matrices for brick-type finite elements because the volume of local finite elements can change during the reanalysis. Consequently, some entries of the mass and stiffness matrices for brick-type finite elements vary highly nonlinearly with respect to geometric variations in the structure. Herein, a novel parameterization technique is proposed to capture these element-level nonlinearities.

Another challenge for MC-PROMs is that they can be numerically not stable due to the transformation matrix they employ. Specifically, the transformation matrix consists of static constraint modes and fixed interface normal modes computed for a set of nominal parameters, and a few sets of perturbed parameter values (typically up to 3 sets per parameter) [13]. If all static constraint modes are kept and many normal modes are included, then the size of the system-level mass and stiffness matrices can be nearly singular (and can even be larger than that of the

full-order models). This is because the transformation matrix can contain vectors which are nearly linearly dependent. These vectors are usually normal modes for substructures where the parametric variation (e.g., modulus of elasticity) does not affect the component-level normal modes. Moreover, the transformation matrix used in MC-PROMs was designed for small parameter variations which ensures that the space spanned by the basis vectors at a component-level does not depend nonlinearly on parameter variations. That approach can break down because of the volume variations which can occur when brick elements are used.

Another challenge of CMS methods and MC-PROMs is that they often require an excessively large number of interface DOFs because (often) these DOFs are many and are hard (or impossible) to reduce. To address this issue, Castanier et al. [6] proposed that the physical interface DOFs be replaced by global interface modes, which were also called characteristic constraint (*CC*) modes. However, this concept is not optimal for substructural-based techniques because *CC* modes are *system*-level interface modes, not *substructural*-level interface modes. Thus, a new technique to reduce the interface DOFs locally is proposed herein and referred to as local-interface reduction.

This paper is organized as follows. In Section 2, the element-level nonlinearity due to the volume variations of finite elements of brick or other type is evaluated, and a novel parameterization technique is proposed to capture this nonlinearity. Next, in Section 3, CMS is briefly reviewed, and next-generation parametric reduced-order models (NX-PROMs) are proposed. In Section 4, to locally reduce the interface DOFs, a local-interface reduction technique is presented. Section 5 discusses the procedure to assemble substructural mass and stiffness matrices (with and without implementing the local-interface reduction technique). In Sec-

tion 6, numerical examples such as a plate structure, an L-shaped structure, and a realistic vehicle model (a high mobility multipurpose wheeled vehicle, HMMWV) modeled with brick-type finite elements are used to demonstrate the proposed methods. Finally, conclusions are summarized in Section 7.

2. Robust Parameterization Techniques for Element-Level Nonlinearity

For structural design and damage modeling purposes, the parameterization of the mass and stiffness matrices can be the most important step. This is because the parameterization techniques enable capturing mass and stiffness variations due to design changes or damage in the structure. Thus, the reanalysis time can be significantly reduced because the finite element mesh does not need to be modified and remodeled. The parameterization technique has to be adapted for the different characteristics of each type of finite element used. For example, the thickness, Young's modulus, and material density variations of shell-type elements can be captured well by third-order Taylor series [8, 9, 12, 13]. However, we found that the thickness variations for a brick and other types of finite elements such as hexagonal and tetrahedron elements cannot be captured well by Taylor series of low order due to an element-level nonlinear characteristics caused by volume variations. For elements which have volume, local thickness variations induce volume variations in the elements. In contrast, Taylor series works well for parameterizing shell-type elements because these do not have actual volume. In this section, a parameterization technique that captures thickness variations of brick and other types of finite elements is the focus.

Fig. 1 shows an 8-node brick-type element which uses first-order (linear) shape functions. Coordinates x , y , and z are global, and coordinates ξ , η , and ζ are local.

As a conceptual example, consider that the four nodes on the top surface in Fig. 1 move by a distance Δt . The brick-type element has a volume, so when each node moves, the volume of the brick-type element varies. Thus, the parameterization technique has to account for these volume variations. To that aim, let us first revisit the formulation used to derive stiffness matrices for brick-type elements [14, 15]. The equation used to obtain the stiffness matrix can be expressed as

$$\begin{aligned}
\mathbf{K} &= \int_V \mathbf{B}^T \mathbf{D} \mathbf{B} dV \\
&= \int_{\zeta=-1}^{\zeta=1} \int_{\eta=-1}^{\eta=1} \int_{\xi=-1}^{\xi=1} \mathbf{B}^T \mathbf{D} \mathbf{B} d\xi d\eta d\zeta \\
&= \sum_{i=1}^8 \sum_{j=1}^8 \sum_{k=1}^8 W_i W_j W_k \mathbf{B}^T(\xi_i, \eta_j, \zeta_k) \mathbf{D} \mathbf{B}(\xi_i, \eta_j, \zeta_k) \det(\mathbf{J}(\xi_i, \eta_j, \zeta_k)),
\end{aligned} \tag{1}$$

where \mathbf{B} is a strain matrix (which contains derivatives of the linear shape functions in global coordinates), and \mathbf{D} is an elasticity matrix (which contains Poisson's ratio ν , and the elastic modulus E). The determinant of the Jacobian in Eq. (1) is obtained from the coordinate transformation of the strain matrix \mathbf{B} . The determinant contains in its denominator a cubic polynomial of ξ , η and ζ , which reflects volume variations. Thus, the parameterization should also contain a cubic polynomial in the denominator. To establish the coefficients of this cubic polynomial, the volume variations of brick-type elements are considered. As shown in Fig. 1, one or several nodes on the top surface move to capture thickness variations. The resulting volume can be expressed as

$$V = V_0 \left[1 + d \frac{p - p_0}{p_0} \right] = V_0 \left(1 + d \frac{\Delta p}{p_0} \right),$$

where V and V_0 are the final and the initial volume of the brick-type element, and p and p_0 are the target parameter value (thickness) and the initial parameter

value. When only one node on the top surface moves, the coefficient d is $1/3$. Similarly, when two nodes move, $d = 1/2$. Also, when three nodes move, $d = 1$. Finally, when four nodes move, the volume variation is proportional to Δp , i.e. $V = V_0 \frac{\Delta p}{p}$. This last type of variation, proportional to Δp , is very well captured by a regular interpolation. The other three cases, however, are not. To address this issue, a cubic polynomial which considers the volume variation of brick-type elements with a target parameter variation Δp is defined as

$$D(\Delta p) = \left(1 + \frac{\Delta p}{p_0}\right) \left(1 + \frac{1}{2} \frac{\Delta p}{p_0}\right) \left(1 + \frac{1}{3} \frac{\Delta p}{p_0}\right). \quad (2)$$

The new parameterization equation consists of a fourth-order interpolation in the numerator and the cubic polynomial in Eq. (2) in the denominator, which yields the new parameterization as

$$\mathbf{K}(p_0 + \Delta p) \approx \frac{\mathbf{K}_0 + \mathbf{K}_1 \Delta p + \mathbf{K}_2 (\Delta p)^2 + \mathbf{K}_3 (\Delta p)^3 + \mathbf{K}_4 (\Delta p)^4}{D(\Delta p)}. \quad (3)$$

To calculate the matrices \mathbf{K}_0 , \mathbf{K}_1 , \mathbf{K}_2 , \mathbf{K}_3 and \mathbf{K}_4 in Eq. (3), five equations are needed. For that, stiffness matrices for five parameter values are computed. First, consider the case where $\Delta p = 0$. One obtains

$$\mathbf{K}(p_0) \approx \mathbf{K}_0. \quad (4)$$

Next, consider $\Delta p = i\delta p$ (with $i = 1, 2, 3, 4$), one obtains

$$\mathbf{K}(p_0 + i\delta p) \approx \frac{\mathbf{K}_0 + \mathbf{K}_1 (i\delta p) + \mathbf{K}_2 (i\delta p)^2 + \mathbf{K}_3 (i\delta p)^3 + \mathbf{K}_4 (i\delta p)^4}{D(i\delta p)}. \quad (5)$$

Rearranging Eqs. (4) and (5) into matrix form, for each entry e, q of the matrices

$\mathbf{K}_1, \mathbf{K}_2, \mathbf{K}_3$ and \mathbf{K}_4 , one obtains

$$\begin{bmatrix} 1 & 0 & 0 & 0 & 0 \\ \frac{1}{D(\delta p)} & \frac{\delta p}{D(\delta p)} & \frac{(\delta p)^2}{D(\delta p)} & \frac{(\delta p)^3}{D(\delta p)} & \frac{(\delta p)^4}{D(\delta p)} \\ \frac{1}{D(2\delta p)} & \frac{2\delta p}{D(2\delta p)} & \frac{(2\delta p)^2}{D(2\delta p)} & \frac{(2\delta p)^3}{D(2\delta p)} & \frac{(2\delta p)^4}{D(2\delta p)} \\ \frac{1}{D(3\delta p)} & \frac{3\delta p}{D(3\delta p)} & \frac{(3\delta p)^2}{D(3\delta p)} & \frac{(3\delta p)^3}{D(3\delta p)} & \frac{(3\delta p)^4}{D(3\delta p)} \\ \frac{1}{D(4\delta p)} & \frac{4\delta p}{D(4\delta p)} & \frac{(4\delta p)^2}{D(4\delta p)} & \frac{(4\delta p)^3}{D(4\delta p)} & \frac{(4\delta p)^4}{D(4\delta p)} \end{bmatrix} \begin{bmatrix} \mathbf{K}_{0,eq} \\ \mathbf{K}_{1,eq} \\ \mathbf{K}_{2,eq} \\ \mathbf{K}_{3,eq} \\ \mathbf{K}_{4,eq} \end{bmatrix} = \begin{bmatrix} \mathbf{K}(p_0)_{eq} \\ \mathbf{K}(p_0 + \delta p)_{eq} \\ \mathbf{K}(p_0 + 2\delta p)_{eq} \\ \mathbf{K}(p_0 + 3\delta p)_{eq} \\ \mathbf{K}(p_0 + 4\delta p)_{eq} \end{bmatrix}. \quad (6)$$

Equation (6) can be easily solved by simply inverting the 5×5 matrix on the left hand side. This matrix is non-singular and very well behaved for inversion. Also, note that this inversion has to be done only once (for a given δp). Let us denote by \mathbf{A} this inverse matrix, i.e.

$$\mathbf{A} = \begin{bmatrix} 1 & 0 & 0 & 0 & 0 \\ \frac{1}{D(\delta p)} & \frac{\delta p}{D(\delta p)} & \frac{(\delta p)^2}{D(\delta p)} & \frac{(\delta p)^3}{D(\delta p)} & \frac{(\delta p)^4}{D(\delta p)} \\ \frac{1}{D(2\delta p)} & \frac{2\delta p}{D(2\delta p)} & \frac{(2\delta p)^2}{D(2\delta p)} & \frac{(2\delta p)^3}{D(2\delta p)} & \frac{(2\delta p)^4}{D(2\delta p)} \\ \frac{1}{D(3\delta p)} & \frac{3\delta p}{D(3\delta p)} & \frac{(3\delta p)^2}{D(3\delta p)} & \frac{(3\delta p)^3}{D(3\delta p)} & \frac{(3\delta p)^4}{D(3\delta p)} \\ \frac{1}{D(4\delta p)} & \frac{4\delta p}{D(4\delta p)} & \frac{(4\delta p)^2}{D(4\delta p)} & \frac{(4\delta p)^3}{D(4\delta p)} & \frac{(4\delta p)^4}{D(4\delta p)} \end{bmatrix}^{-1} = \begin{bmatrix} A_{11} & A_{12} & A_{13} & A_{14} & A_{15} \\ A_{21} & A_{22} & A_{23} & A_{24} & A_{25} \\ A_{31} & A_{32} & A_{33} & A_{34} & A_{35} \\ A_{41} & A_{42} & A_{43} & A_{44} & A_{45} \\ A_{51} & A_{52} & A_{53} & A_{54} & A_{55} \end{bmatrix}. \quad (7)$$

Re-arranging Eq. (6) using the entries in \mathbf{A} , one obtains

$$\begin{aligned} \mathbf{K}(p_0 + \Delta p) &\approx (A_{11} + A_{21}\Delta p + A_{31}\Delta p^2 + A_{41}\Delta p^3 + A_{51}\Delta p^4)\mathbf{K}(p_0) \\ &+ (A_{12} + A_{22}\Delta p + A_{32}\Delta p^2 + A_{42}\Delta p^3 + A_{52}\Delta p^4)\mathbf{K}(p_0 + \delta p) \\ &+ (A_{13} + A_{23}\Delta p + A_{33}\Delta p^2 + A_{43}\Delta p^3 + A_{53}\Delta p^4)\mathbf{K}(p_0 + 2\delta p) \\ &+ (A_{14} + A_{24}\Delta p + A_{34}\Delta p^2 + A_{44}\Delta p^3 + A_{54}\Delta p^4)\mathbf{K}(p_0 + 3\delta p) \\ &+ (A_{15} + A_{25}\Delta p + A_{35}\Delta p^2 + A_{45}\Delta p^3 + A_{55}\Delta p^4)\mathbf{K}(p_0 + 4\delta p), \text{ or} \\ \mathbf{K}(p_0 + \Delta p) &\approx b_0\mathbf{K}(p_0) + b_1\mathbf{K}(p_0 + \delta p) + b_2\mathbf{K}(p_0 + 2\delta p) \\ &+ b_3\mathbf{K}(p_0 + 3\delta p) + b_4\mathbf{K}(p_0 + 4\delta p). \end{aligned} \quad (8)$$

Equation (8) shows that $\mathbf{K}(p_0 + \Delta p)$ is simply a linear combination of five (pre-computed) matrices. The coefficients in the linear combination depend very non-linearly on Δp . That is the key factor which ensures the high accuracy of the new parameterization. Note that the computational cost of the new parameterization is the same as that for a regular fourth-order interpolation. The accuracy, however, is higher (as shown on Section 6.1).

3. Reduced-Order Models

The parameterization techniques proposed in Section 2 are for the full-order finite element model. However, the main objective of this work is to predict vibration responses using ROMs (as opposed to full-order models) to reduce the calculation time. To detail the construction of ROMs, the fixed-interface Craig-Bampton component mode synthesis (CB-CMS) [5] is reviewed briefly. Next, a new transformation matrix is presented and used in conjunction with the new parameterization technique discussed in Section 2. Finally, NX-PROMs are constructed.

3.1. Brief review of Craig-Bampton component mode synthesis

In this section, the fixed-interface CB-CMS [2] method is reviewed. This modeling approach is broadly used because of its simplicity and computational stability. To apply the CB-CMS, the complex structure of interest is partitioned into substructures. The DOFs of each substructure are further partitioned into active DOFs on the interface (indicated by the superscript A), and omitted DOFs in the interior (indicated by the superscript O). The mass and stiffness matrices

for a component i can then be partitioned to obtain

$$\mathbf{M}_i = \begin{bmatrix} \mathbf{m}_i^{AA} & \mathbf{m}_i^{AO} \\ \mathbf{m}_i^{OA} & \mathbf{m}_i^{OO} \end{bmatrix}, \quad \text{and} \quad \mathbf{K}_i = \begin{bmatrix} \mathbf{k}_i^{AA} & \mathbf{k}_i^{AO} \\ \mathbf{k}_i^{OA} & \mathbf{k}_i^{OO} \end{bmatrix}.$$

Next, the physical coordinates are changed to a set of coordinates representing the amplitudes of a selected set of fixed-interface component-level normal modes Φ_i^N (indicated by the superscript N), and the amplitudes of the full set of static constraint modes $\Phi_i^C = -\mathbf{k}_i^{OO^{-1}}\mathbf{k}_i^{OA}$ (indicated by the superscript C). The transformed mass and stiffness matrices for component i can be expressed as

$$\mathbf{M}_i^{CBCMS} = \begin{bmatrix} \hat{\mathbf{m}}_i^C & \hat{\mathbf{m}}_i^{CN} \\ \hat{\mathbf{m}}_i^{NC} & \hat{\mathbf{m}}_i^N \end{bmatrix}, \quad \text{and} \quad \mathbf{K}_i^{CBCMS} = \begin{bmatrix} \hat{\mathbf{k}}_i^C & \hat{\mathbf{k}}_i^{CN} \\ \hat{\mathbf{k}}_i^{NC} & \hat{\mathbf{k}}_i^N \end{bmatrix}.$$

In this work, the CB-CMS method is used *only* for the substructures which do not have any parameter variation or damage.

3.2. Next-generation parametric reduced-order models

In this section, MC-PROMs are improved to be more robust and mathematically stable. The resulting models are referred to as NX-PROMs.

3.2.1. Transformation matrix for NX-PROMs

The transformation matrix for NX-PROMs is constructed somewhat similar to MC-PROMs (which was constructed by using the idea behind CB-CMS). It also has a set of static constraint modes Ψ^C and a set of fixed-interface normal modes Φ^N . However, the transformation matrix for NX-PROMs has a different set of static constraint modes and a different set of fixed-interface normal modes compared at CB-CMS and MC-PROM. This transformation matrix can be written

for component i as

$$\mathbf{T}_i = \begin{bmatrix} \mathbf{I} & \mathbf{0} \\ \boldsymbol{\Psi}_{\text{aug},i}^C & \boldsymbol{\Phi}_{\text{aug},i}^N \end{bmatrix},$$

where $\boldsymbol{\Psi}_{\text{aug}}^C$ is referred to as the matrix of augmented constraint modes

$$\boldsymbol{\Psi}_{\text{aug},i}^C = \begin{bmatrix} \boldsymbol{\Psi}_{0,i}^C & \boldsymbol{\Psi}_{1,i}^C & \boldsymbol{\Psi}_{2,i}^C & \boldsymbol{\Psi}_{3,i}^C & \boldsymbol{\Psi}_{4,i}^C \end{bmatrix},$$

and $\boldsymbol{\Phi}_{\text{aug}}^N$ is referred to as the matrix of augmented fixed-interface normal modes

$$\boldsymbol{\Phi}_{\text{aug},i}^N = \begin{bmatrix} \boldsymbol{\Phi}_{0,i}^N & \boldsymbol{\Phi}_{1,i}^N & \boldsymbol{\Phi}_{2,i}^N & \boldsymbol{\Phi}_{3,i}^N & \boldsymbol{\Phi}_{4,i}^N \end{bmatrix}.$$

Matrices $\boldsymbol{\Psi}_{0,i}^C$ and $\boldsymbol{\Phi}_{0,i}^N$ correspond to the nominal parameter values, whereas matrices $\boldsymbol{\Psi}_{l,i}^C$ and $\boldsymbol{\Phi}_{l,i}^N$ ($l = 1, 2, 3, 4$) correspond to four other parameter values.

In general, the columns of $\boldsymbol{\Phi}_{\text{aug}}^N$ are not orthogonal. Therefore, for numerical stability, an orthogonal basis for the space spanned by these modes is computed. This basis is obtained by a truncated set of left singular vectors \mathbf{U}^N of $\boldsymbol{\Phi}_{\text{aug}}^N$ [13]. Thus, the new transformation matrix can be expressed as

$$\tilde{\mathbf{T}}_i = \begin{bmatrix} \mathbf{I} & \mathbf{0} \\ \boldsymbol{\Psi}_{\text{aug},i}^C & \mathbf{U}_i^N \end{bmatrix}. \quad (9)$$

The transformation matrix in Eq. (9) can be used to project the physical domain onto the NX-PROM domain. The stiffness matrix $\mathbf{K}_i^{NX\text{PROM}} = \tilde{\mathbf{T}}_i^T \mathbf{K}_i^{FEM} \tilde{\mathbf{T}}_i$ for component i (where \mathbf{K}_i^{FEM} represents the stiffness matrix of the full-order model

of component i) can be partitioned to obtain

$$\mathbf{K}_i^{NXPROM} = \begin{bmatrix} \mathbf{K}_{00,i}^C & \mathbf{K}_{01,i}^C & \mathbf{K}_{02,i}^C & \mathbf{K}_{03,i}^C & \mathbf{K}_{04,i}^C & \mathbf{K}_{00,i}^{CN} \\ \mathbf{K}_{10,i}^C & \mathbf{K}_{11,i}^C & \mathbf{K}_{12,i}^C & \mathbf{K}_{13,i}^C & \mathbf{K}_{14,i}^C & \mathbf{K}_{11,i}^{CN} \\ \mathbf{K}_{20,i}^C & \mathbf{K}_{21,i}^C & \mathbf{K}_{22,i}^C & \mathbf{K}_{23,i}^C & \mathbf{K}_{24,i}^C & \mathbf{K}_{22,i}^{CN} \\ \mathbf{K}_{30,i}^C & \mathbf{K}_{31,i}^C & \mathbf{K}_{32,i}^C & \mathbf{K}_{33,i}^C & \mathbf{K}_{34,i}^C & \mathbf{K}_{33,i}^{CN} \\ \mathbf{K}_{40,i}^C & \mathbf{K}_{41,i}^C & \mathbf{K}_{42,i}^C & \mathbf{K}_{43,i}^C & \mathbf{K}_{44,i}^C & \mathbf{K}_{44,i}^{CN} \\ \mathbf{K}_{00,i}^{NC} & \mathbf{K}_{11,i}^{NC} & \mathbf{K}_{22,i}^{NC} & \mathbf{K}_{33,i}^{NC} & \mathbf{K}_{44,i}^{NC} & \mathbf{K}_i^N \end{bmatrix}.$$

A similar relation is obtained for the mass matrix of component i . Here, the DOFs corresponding to the constraint part (superscript C) are repeated for the five parameter values (denoted by subscript 0, 1, 2, 3 and 4). Note that in such an approach, the size of the mass and stiffness matrices can be quite large. Also, these matrices may be ill-conditioned because the columns of $\Psi_{aug,i}^C$ are not necessarily linearly independent.

To address this issue, a new method to account for the static constraint modes is developed. This new method avoids duplicating the interface DOFs (C) and captures the interface effects more accurately. The approach reduces the number of sets of static constraint modes (used to obtain \mathbf{M}_i^{NXPROM} and \mathbf{K}_i^{NXPROM}) from five sets to just one set. Consider that the actual value p of the parameter where the reanalysis is needed exists between the l^{th} and $(l + 1)^{\text{th}}$ parameter values ($l = 0, 1, 2, 3$ or 4) which were used to construct \mathbf{M}_i^{NXPROM} . In that case (described in Fig. 2), a new static constraint mode can be generated by linearly interpolating between the static constraint modes for the l^{th} and the $(l + 1)^{\text{th}}$ parameter values to obtain

$$\tilde{\Psi}_i^C = \left(\frac{pl_{+1} - p}{pl_{+1} - pl} \right) \Psi_{l,i}^C + \left(\frac{p - pl}{pl_{+1} - pl} \right) \Psi_{l+1,i}^C = \alpha_i \Psi_{l,i}^C + \beta_i \Psi_{l+1,i}^C. \quad (10)$$

This new static constraint mode $\tilde{\Psi}_i^C$ replaces all five static constraint modes used to construct $\tilde{\mathbf{T}}_i$ in Eq. (9).

Note that this reduction can be implemented without re-constructing $\tilde{\mathbf{T}}_i$ for each case of parameter variation. Instead, only simple linear combinations of partitions of the matrices \mathbf{M}_i^{NXPROM} and \mathbf{K}_i^{NXPROM} , are needed. Details are given in Section 3.2.2 below. In the end, the final NX-PROM mass and stiffness matrices have only a single set of constraint modes $\tilde{\Psi}_i^C$ which always has linearly independent columns.

3.2.2. parameterization for NX-PROMs

The new interpolation presented in Section 2 is applied to NX-PROMs. To that aim, five mass and five stiffness are constructed for each component i (for $l = 0, 1, 2, 3, 4$) as follows

$$\mathbf{M}_{l,i}^{NX} = \tilde{\mathbf{T}}_i^T \mathbf{M}(p_0 + l\delta p) \tilde{\mathbf{T}}_i \quad \text{and} \quad \mathbf{K}_{l,i}^{NX} = \tilde{\mathbf{T}}_i^T \mathbf{K}(p_0 + l\delta p) \tilde{\mathbf{T}}_i.$$

These matrices are not all used independently to form NX-PROMs. Instead, they are linearly combined to implement the single set of static constraint modes $\tilde{\Psi}_i^C$ in Eq. (10). Thus, conceptually, $\tilde{\mathbf{T}}_i$ is replaced by $\hat{\mathbf{T}}_i$, given by

$$\hat{\mathbf{T}}_i = \begin{bmatrix} \mathbf{I} & \mathbf{0} \\ \boldsymbol{\Psi}_{\text{aug},i}^C & \mathbf{U}_i^N \end{bmatrix} (\alpha_i \mathbf{R}_{l,i} + \beta_i \mathbf{R}_{l+1,i}) = \tilde{\mathbf{T}} (\alpha_i \mathbf{R}_{l,i} + \beta_i \mathbf{R}_{l+1,i}),$$

where $\mathbf{R}_{l,i}$ and $\mathbf{R}_{l+1,i}$ are masking matrices of zeros and ones. The matrix $\mathbf{R}_{l,i}$ is a 6×2 block matrix where the blocks $(l, 1)$ and $(6, 2)$ are unit matrices, while all other blocks are zero. The first five rows correspond to $\boldsymbol{\Psi}_{l,i}^C$ ($l = 0, 1, 2, 3, 4$) and the last row corresponds to \mathbf{U}_i^N . This new transformation matrix $\hat{\mathbf{T}}_i$ is applied to the mass and stiffness matrices of component i to construct NX-PROMs. First,

five mass and stiffness matrices are constructed for each parameter variation $s\delta p$ (for $s = 0, 1, 2, 3, 4$) as follows

$$\begin{aligned}\hat{\mathbf{M}}_{s,i}^{NX} &= (\alpha_i \mathbf{R}_{l,i}^T + \beta_i \mathbf{R}_{l+1,i}^T) \mathbf{M}_{s,i}^{NX} (\alpha_i \mathbf{R}_{l,i} + \beta_i \mathbf{R}_{l+1,i}), \\ \hat{\mathbf{K}}_{s,i}^{NX} &= (\alpha_i \mathbf{R}_{l,i}^T + \beta_i \mathbf{R}_{l+1,i}^T) \mathbf{K}_{s,i}^{NX} (\alpha_i \mathbf{R}_{l,i} + \beta_i \mathbf{R}_{l+1,i}).\end{aligned}$$

Next, the new interpolation discussed in Section 2 is applied using $\hat{\mathbf{M}}_{s,i}^{NX}$ and $\hat{\mathbf{K}}_{s,i}^{NX}$. Eq. (8) is used to obtain

$$\begin{aligned}\mathbf{M}(p_0 + \Delta p)_i^{NX} &\approx b_0 \hat{\mathbf{M}}_{0,i}^{NX} + b_1 \hat{\mathbf{M}}_{1,i}^{NX} + b_2 \mathbf{M}_{2,i}^{NX} + b_3 \hat{\mathbf{M}}_{3,i}^{NX} + b_4 \hat{\mathbf{M}}_{4,i}^{NX} \\ \mathbf{K}(p_0 + \Delta p)_i^{NX} &\approx b_0 \hat{\mathbf{K}}_{0,i}^{NX} + b_1 \hat{\mathbf{K}}_{1,i}^{NX} + b_2 \mathbf{K}_{2,i}^{NX} + b_3 \hat{\mathbf{K}}_{3,i}^{NX} + b_4 \hat{\mathbf{K}}_{4,i}^{NX}\end{aligned}$$

where b_s ($s = 0, 1, 2, 3, 4$) are computed for each Δp by using the matrix \mathbf{A} and the expression in Eq. (8). Note that the five coefficients b_s which depend on the actual Δp are easily calculated because they are just five scalars that depend only on Δp and δp irrespective of the size of the finite element mesh.

Finally, the mass and stiffness matrices for the i^{th} component of the NX-PROMs can be partitioned as follows

$$\begin{aligned}\mathbf{M}(p_0 + \Delta p)_i^{NX} &= \begin{bmatrix} \mathbf{M}_{\Delta p,i}^C & \mathbf{M}_{\Delta p,i}^{CN} \\ \mathbf{M}_{\Delta p,i}^{NC} & \mathbf{M}_{\Delta p,i}^N \end{bmatrix}, \\ \mathbf{K}(p_0 + \Delta p)_i^{NX} &= \begin{bmatrix} \mathbf{K}_{\Delta p,i}^C & \mathbf{K}_{\Delta p,i}^{CN} \\ \mathbf{K}_{\Delta p,i}^{NC} & \mathbf{K}_{\Delta p,i}^N \end{bmatrix},\end{aligned}\tag{11}$$

where superscript C indicates a constraint partition, and superscript N indicates a nominal mode partition.

4. Local-Interface Reduction

If the finite element mesh used is very fine, the size of the reduced system-level matrices is dominated by the constraint DOFs corresponding to the C partition in

Eq. (11). The constraint DOFs of matrices constructed by CMS-based techniques are difficult to reduce. This is an important issue because, if the constraint DOFs cannot be reduced, then the overall structure cannot be efficiently divided into many substructures. To address this issue, Castanier et al. [6] suggested the use of characteristic constraint (CC) modes. This technique is based on performing a secondary eigenanalysis of the constraint partition (C) of the system-level mass and stiffness matrices constructed by CB-CMS. This technique is applied after the system-level matrices are constructed. However, the core idea of NX-PROMs is that all analyses are accomplished at the substructure-level, and not at the system-level. Thus, an alternate interface reduction technique is proposed next. The new approach is applied at the substructure-level, and it is referred to as local-interface reduction (LIR).

The local-interface reduction technique is also based on a secondary eigenanalysis of the constraint partition. However, the secondary eigenanalysis is executed on the constraint partitions (C) of the substructural matrices, not the system-level matrices. The secondary eigenanalyses on constraint DOFs (C) of the mass and stiffness matrices of component i constructed by either CB-CMS or the NX-PROM approach are given by

$$\mathbf{K}_{\Delta p,i}^C \Phi_{\Delta p,i}^{CC} - \mathbf{M}_{\Delta p,i}^C \Phi_{\Delta p,i}^{CC} \Lambda_{\Delta p,i} = \mathbf{0},$$

where $\Lambda_{\Delta p,i}$ is a diagonal matrix which contains the eigenvalues, and $\Phi_{\Delta p,i}^{CC}$ are the characteristic constraint (CC) modes of the i^{th} substructure. They are truncated for the frequency range of interest by using the eigenvalues in $\Lambda_{\Delta p,i}$. The rows of the CC modes indicate the constraint DOFs of the substructure, and the columns represent the set of truncated CC modes. The CC modes for each substructure are used to reduce the interface DOFs *for each boundary locally*. Note that joining all

CC modes for each interface between different components may lead to vectors which are not necessarily linearly independent. However, they span the adequate space. Thus, the left singular values of the CC interface modes may have to be used for certain interfaces. To demonstrate the LIR procedure, a simple plate model is used in Section 6.2.

The set of orthogonal basis vectors used for all interfaces that a component i has with other components are grouped in a block diagonal matrix which contains the entire interface component i has. The number of blocks is equal to the number of components that are connected to component i . These matrices are denoted by $\mathbf{U}_{\Delta p,i}$. Of course, if component i connects to only one other component, then there is only one block in $\mathbf{U}_{\Delta p,i}$. Next, the mass and stiffness matrices in Eq. (11) are projected using $\mathbf{U}_{\Delta p,i}$ as follows

$$\begin{aligned} \mathbf{M}_{\Delta p,i}^{CC} &= \mathbf{U}_{\Delta p,i}^T \mathbf{M}_{\Delta p,i}^C \mathbf{U}_{\Delta p,i}, & \mathbf{M}_{\Delta p,i}^{CCN} &= \mathbf{U}_{\Delta p,i}^T \mathbf{M}_{\Delta p,i}^{CN}, & \mathbf{M}_{\Delta p,i}^{NCC} &= \mathbf{M}_{\Delta p,i}^{CN} \mathbf{U}_{\Delta p,i}, \\ \mathbf{K}_{\Delta p,i}^{CC} &= \mathbf{U}_{\Delta p,i}^T \mathbf{K}_{\Delta p,i}^C \mathbf{U}_{\Delta p,i}, & \mathbf{K}_{\Delta p,i}^{CCN} &= \mathbf{U}_{\Delta p,i}^T \mathbf{K}_{\Delta p,i}^{CN}, & \mathbf{K}_{\Delta p,i}^{NCC} &= \mathbf{K}_{\Delta p,i}^{CN} \mathbf{U}_{\Delta p,i}. \end{aligned} \quad (12)$$

Thus, the final mass and stiffness matrices with reduced constraint DOFs are given for component i by

$$\mathbf{M}_{\Delta p,i}^{LIR} = \begin{bmatrix} \mathbf{M}_{\Delta p,i}^{CC} & \mathbf{M}_{\Delta p,i}^{CCN} \\ \mathbf{M}_{\Delta p,i}^{NCC} & \mathbf{M}_{\Delta p,i}^N \end{bmatrix}, \quad \mathbf{K}_{\Delta p,i}^{LIR} = \begin{bmatrix} \mathbf{K}_{\Delta p,i}^{CC} & \mathbf{K}_{\Delta p,i}^{CCN} \\ \mathbf{K}_{\Delta p,i}^{NCC} & \mathbf{K}_{\Delta p,i}^N \end{bmatrix},$$

where superscript LIR indicates that the matrices are constructed using local-interface reduction. An example is provided in Section 6.2.

5. Assembly

To predict the system-level dynamics, the mass and stiffness matrices obtained in Sections 3 and 4 for each substructure have to be assembled. To do that, ge-

ometric compatibility conditions must be enforced. In the following, we discuss separately the case where LIR is not used and the case where it is used.

Let us consider the case where the geometric compatibility conditions are used for models without LIR. In this case, the constraint partitions (C) of component-level matrices keep the meaning of the physical interface DOFs of matrices obtained from FEMs. This means that the geometric compatibility conditions between interface DOFs (constraint DOFs) can be applied directly to construct the system-level matrices. The complete component-level equations of motion for component i based on CB-CMS or the NX-PROM approach can be expressed as

$$\mathbf{M}_i^{ROM} \ddot{\mathbf{q}}_i^{ROM} + \mathbf{K}_i^{ROM} \mathbf{q}_i^{ROM} = \mathbf{F}_i^{ROM}, \quad (13)$$

where ROM indicates component-level matrices obtained using either CB-CMS or the NX-PROM approach. The stiffness matrices in Eq. (13) obtained for components without parameter variability can be expressed as

$$\mathbf{K}_i^{ROM} = \mathbf{K}_i^{CBCMS} = \begin{bmatrix} \mathbf{K}_i^C & \mathbf{K}_i^{CN} \\ \mathbf{K}_i^{NC} & \mathbf{K}_i^N \end{bmatrix}^{CBCMS}. \quad (14)$$

For component with parameter variability, the stiffness matrices in Eq. (13) can be expressed as

$$\mathbf{K}_i^{ROM} = \mathbf{K}_i^{NX} = \begin{bmatrix} \mathbf{K}_{\Delta p, i}^C & \mathbf{K}_{\Delta p, i}^{CN} \\ \mathbf{K}_{\Delta p, i}^{NC} & \mathbf{K}_{\Delta p, i}^N \end{bmatrix}^{NX PROM}. \quad (15)$$

The formulas for the mass matrices are similar to those for the system matrices in Eqs. (14) and (15) (and are omitted here for the sake of brevity).

Next, the matrices in Eq. (13) are grouped for all i to obtain

$$\begin{aligned}\hat{\mathbf{M}} &= \mathbf{Bdiag} \left[\mathbf{M}_1^{ROM} \quad \dots \quad \mathbf{M}_n^{ROM} \right], \\ \hat{\mathbf{K}} &= \mathbf{Bdiag} \left[\mathbf{K}_1^{ROM} \quad \dots \quad \mathbf{K}_n^{ROM} \right], \\ \hat{\mathbf{F}} &= \left[\mathbf{F}_1^{ROM^T} \quad \dots \quad \mathbf{F}_n^{ROM^T} \right]^T,\end{aligned}\tag{16}$$

where n is the number of components, and $\mathbf{Bdiag}[\cdot]$ denotes a block-diagonal matrix.

The geometric compatibility condition for the ROM is expressed as

$$\mathbf{q}_i^C = \mathbf{q}_j^C,\tag{17}$$

where, \mathbf{q}_i and \mathbf{q}_j are the generalized coordinates for the constraint partitions (C for CB-CMS or NX-PROMs) that correspond to the interface between components i and j . Of course, there is no compatibility condition to be enforced for two components which do not have a common interface.

Equation (17) is used to transform the matrices in Eq. (16) similar to the assembly process in all finite element modeling methods. The final assembled, reduced-order, system-level matrices are given by

$$\begin{aligned}\mathbf{M}_{sys}^{ROM} &= \begin{bmatrix} \mathbf{M}^C & \mathbf{M}^{CN} \\ \mathbf{M}^{NC} & \mathbf{M}^N \end{bmatrix}, \mathbf{K}_{sys}^{ROM} = \begin{bmatrix} \mathbf{K}^C & \mathbf{K}^{CN} \\ \mathbf{K}^{NC} & \mathbf{K}^N \end{bmatrix}, \\ \mathbf{F}_{sys}^{ROM} &= \begin{bmatrix} \mathbf{F}^C \\ \mathbf{F}^N \end{bmatrix},\end{aligned}$$

where

$$\mathbf{K}^{CN} = \begin{bmatrix} \mathbf{K}_1^{CN} & \mathbf{K}_2^{CN} & \dots & \mathbf{K}_n^{CN} \end{bmatrix}, \quad \mathbf{K}^{NC} = \mathbf{K}^{CN\text{T}},$$

$$\mathbf{K}^N = \begin{bmatrix} \mathbf{K}_1^N & \mathbf{0} & \dots & \mathbf{0} \\ \mathbf{0} & \mathbf{K}_2^N & \dots & \mathbf{0} \\ \vdots & \vdots & \ddots & \mathbf{0} \\ \mathbf{0} & \mathbf{0} & \dots & \mathbf{K}_n^N \end{bmatrix},$$

and \mathbf{K}^C is a matrix which is obtained by the assembly of each interface. In general, \mathbf{K}^C is a matrix which has a smaller size than the C partitions in $\hat{\mathbf{K}}$. The same process is applied to obtain \mathbf{F}^C . Also, similar relations are obtained for the mass matrix \mathbf{M}_{sys}^{ROM} (and are omitted here for the sake of brevity).

Finally, the compatibility conditions for models constructed using LIR can be expressed almost identically to those for models without LIR. The only difference is that the generalized coordinates in Eq. (17) represent amplitudes of characteristic constraint modes or amplitudes of the basis vectors used to capture the space spanned by the characteristic constraint modes.

6. Numerical Results

6.1. Element-level nonlinearity of brick and other types of finite elements

Figure (3) shows a simple plate structure modeled with a shell-type finite elements, where t is the thickness of the plate ($t = 0.2 \text{ mm}$). To examine the variation in the entries of the finite element mass and stiffness matrices for this substructure, the thickness t is varied by increments of $\Delta t = 0.01 \text{ mm}$.

The size of the mass and stiffness matrices of the simple structure shown in Fig. 3 is $15,582 \times 15,582$. As an example, the 32nd diagonal entries of the mass

and stiffness matrices, $\mathbf{M}_{32,32}$ and $\mathbf{K}_{32,32}$, are shown in Fig. 4 as the thickness varies (approximated matrices are shown by a dash-dot line, and the actual matrices are shown by a solid-line for various values of Δp). One may observe that those entries of the mass and stiffness matrices vary almost linearly. To capture these variations very accurately, a cubic interpolation is used as follows

$$\mathbf{K}(p_0 + \Delta p) \approx \tilde{\mathbf{K}}_0 + \tilde{\mathbf{K}}_1 \Delta p + \tilde{\mathbf{K}}_2 \Delta p^2 + \tilde{\mathbf{K}}_3 \Delta p^3. \quad (18)$$

The matrices $\tilde{\mathbf{K}}_0$, $\tilde{\mathbf{K}}_1$, $\tilde{\mathbf{K}}_2$, and $\tilde{\mathbf{K}}_3$ are computed by using the stiffness matrices evaluated at three parameter values. These values are the reference value p_0 , the first perturbed value $p_1 = p_0 + \delta p$, the second perturbed value $p_2 = p_0 + 2\delta p$ and the third perturbed value $p_3 = p_0 + 3\delta p$. The procedure is standard and similar to the one used in Section 2, so its details are omitted here for the sake of brevity. A similar interpolation is used for the mass matrix. Note that, in contrast to Taylor series, the cubic interpolation does not require the calculation of derivative terms.

Next, to examine the variations in the entries of the mass and stiffness matrices for brick-type elements, the same plate structure is modeled with brick-type elements. The nominal thickness of the plate is (the same) 0.2 mm and is varied by (the same) increments of $\Delta t = 0.01 \text{ mm}$, as shown in Fig. 5. The thickness is varied in a region near the center of the plate. The entries of the mass and stiffness matrices near the DOFs where the thickness is varied are affected. A sample DOF affected is the 645th. The 645th diagonal entry of the mass matrix varies linearly (and is omitted for the sake of brevity). The same entry of the stiffness matrix, however, does not vary linearly, as shown in Fig. 6 (left), where exact values are shown by a solid-line. To capture this nonlinear variation, the cubic interpolation function in Eq. (18) is used. The approximate values obtained are shown by a dash-dot line. These results show that Eq. (18) is not good enough to capture

the highly nonlinear variation of the stiffness matrix. Therefore, a fourth-order interpolation is used as follows

$$\mathbf{K}(p_0 + \Delta p) \approx \tilde{\mathbf{K}}_0 + \tilde{\mathbf{K}}_1 \Delta p + \tilde{\mathbf{K}}_2 \Delta p^2 + \tilde{\mathbf{K}}_3 \Delta p^3 + \tilde{\mathbf{K}}_4 \Delta p^4. \quad (19)$$

This fourth-order interpolation captures well the nonlinear variation in the entries of the stiffness matrix as shown in Fig. 6 (right).

Based on the results in Fig. 6, one may assume that the errors obtained based on Eq. (19) are negligible. However, that is not correct, as demonstrated by the forced response of the plate calculated using exact and approximated matrices. Figure (7) shows the forced response at one of the DOFs on the plate for excitation frequencies near the first resonance. The solid-line represents the response computed by the actual mass and stiffness matrices, and the dash-dot line indicates the response computed by the mass and stiffness matrices parametrized using Eq. (19) for the case of $\Delta t = 0.37 \text{ mm}$. Clearly, the forced response computed by the parametrized mass and stiffness matrices does not agree with that computed by the actual matrices. This means that the errors in the entries of the stiffness matrix from the fourth-order interpolation are not small enough to capture accurately the dynamic response of the structure with a modified thickness. Note that, the errors in the dynamic response are induced by inaccuracies in the stiffness matrix, not in the mass matrix. These results demonstrated that a new parameterization technique focused on capturing element-level nonlinear variations in the stiffness is needed for brick-type finite elements.

The parametrized stiffness matrix was calculated using Eq. (8) for $\Delta p = 0.37 \text{ mm}$. As a sample of results, Fig. 8 shows that the 645th diagonal entry of the exact and the approximated stiffness matrices match extremely well. Similar matches are observed for all entries of the matrices. Next, forced responses were

calculated using these matrices. The results are shown in Fig. 9. The solid-line indicates the response computed using the exact matrices, and the dash-dot line indicates the response computed by using the new parametrized matrices. The results closely match. Moreover, the natural frequencies for the exact matrices and the new parametrized matrices, match also, as shown in Table 1.

6.2. Example of local-interface reduction

Consider a structure composed of 5 substructures and 3 boundaries as shown in Fig. 10. Γ_j represents the j^{th} boundary. First, using the constraint partitions (C) of the reduced mass and stiffness matrices, the CC modes are computed. These are $\Phi_{\Delta p,1}^{CC}$, $\Phi_{\Delta p,2}^{CC}$, $\Phi_{\Delta p,3}^{CC}$, $\Phi_{\Delta p,4}^{CC}$ and $\Phi_{\Delta p,5}^{CC}$. $\Phi_{\Delta p,1}^{CC}$ has interface DOFs for boundary Γ_1 and Γ_2 , while $\Phi_{\Delta p,2}^{CC}$ has interface DOFs for Γ_2 and Γ_3 . Substructures 3, 4 and 5 each have one boundary Γ_1 , Γ_2 , and Γ_3 , respectively. The mathematical representation for these partitions for each CC mode can be expressed as

$$\begin{aligned} \Phi_{\Delta p,1}^{CC} &= \begin{bmatrix} (\Phi_{\Delta p,1}^{CC})^{\Gamma_1} \\ (\Phi_{\Delta p,1}^{CC})^{\Gamma_2} \end{bmatrix}, \quad \Phi_{\Delta p,2}^{CC} = \begin{bmatrix} (\Phi_{\Delta p,2}^{CC})^{\Gamma_2} \\ (\Phi_{\Delta p,2}^{CC})^{\Gamma_3} \end{bmatrix}, \\ \Phi_{\Delta p,3}^{CC} &= (\Phi_{\Delta p,3}^{CC})^{\Gamma_1}, \quad \Phi_{\Delta p,4}^{CC} = (\Phi_{\Delta p,4}^{CC})^{\Gamma_2}, \quad \Phi_{\Delta p,5}^{CC} = (\Phi_{\Delta p,5}^{CC})^{\Gamma_3}. \end{aligned}$$

By using each boundary partition of the CC modes, the augmented set of CC modes for each boundary is constructed as

$$\begin{aligned} \Phi_{\Delta p,\text{aug}}^{\Gamma_1} &= \begin{bmatrix} (\Phi_{\Delta p,1}^{CC})^{\Gamma_1} & (\Phi_{\Delta p,3}^{CC})^{\Gamma_1} \end{bmatrix}, \\ \Phi_{\Delta p,\text{aug}}^{\Gamma_2} &= \begin{bmatrix} (\Phi_{\Delta p,1}^{CC})^{\Gamma_2} & (\Phi_{\Delta p,2}^{CC})^{\Gamma_2} & (\Phi_{\Delta p,4}^{CC})^{\Gamma_2} \end{bmatrix}, \\ \Phi_{\Delta p,\text{aug}}^{\Gamma_3} &= \begin{bmatrix} (\Phi_{\Delta p,2}^{CC})^{\Gamma_3} & (\Phi_{\Delta p,5}^{CC})^{\Gamma_3} \end{bmatrix}. \end{aligned} \tag{20}$$

Equation (20) describes the augmented CC bases for boundaries Γ_1 , Γ_2 , and Γ_3 . However, the augmented bases $\Phi_{\Delta p,\text{aug}}^{\Gamma_1}$, $\Phi_{\Delta p,\text{aug}}^{\Gamma_2}$, and $\Phi_{\Delta p,\text{aug}}^{\Gamma_3}$ are not guaranteed

to be linearly independent. Thus, they cannot be directly used to reduce the constraint DOFs because of lack of numerical stability. Thus, an orthogonal basis for the space spanned by the augmented CC basis is used. Specifically, the left singular vectors $\tilde{\mathbf{U}}_{\Delta p}^{\Gamma_1}$, $\tilde{\mathbf{U}}_{\Delta p}^{\Gamma_2}$ and $\tilde{\mathbf{U}}_{\Delta p}^{\Gamma_3}$ of the three augmented CC bases $\Phi_{\Delta p, \text{aug}}^{\Gamma_1}$, $\Phi_{\Delta p, \text{aug}}^{\Gamma_2}$, and $\Phi_{\Delta p, \text{aug}}^{\Gamma_3}$ in Eq. (20) are computed for each substructure, and the left singular vector corresponding to singular values larger than 0.01% of the maximum singular value are selected for each boundary. The rows of the orthogonal bases $\tilde{\mathbf{U}}_{\Delta p}^{\Gamma_1}$, $\tilde{\mathbf{U}}_{\Delta p}^{\Gamma_2}$ and $\tilde{\mathbf{U}}_{\Delta p}^{\Gamma_3}$ are (re)sorted for each substructure to match the interface DOFs for each boundary. The resorted matrices are denoted by $\mathbf{U}_{\Delta p}^{\Gamma_1}$, $\mathbf{U}_{\Delta p}^{\Gamma_2}$ and $\mathbf{U}_{\Delta p}^{\Gamma_3}$. The (re)sorted matrices are grouped for each component i to obtain matrices $\mathbf{U}_{\Delta p, i}$ which $\mathbf{U}_{\Delta p, i}$ are used to project the interface DOFs onto the secondary generalized coordinates (CC domain). For example, substructure 1 includes the Γ_1 and Γ_2 boundaries. To reduce the interface DOFs of substructure 1, the orthogonal bases $\mathbf{U}_{\Delta p}^{\Gamma_1}$ and $\mathbf{U}_{\Delta p}^{\Gamma_2}$ are grouped in a matrix $\mathbf{U}_{\Delta p, 1}$ given by

$$\mathbf{U}_{\Delta p, 1} = \begin{bmatrix} \mathbf{U}_{\Delta p}^{\Gamma_1} & \mathbf{0}^{\Gamma_1} \\ \mathbf{0}^{\Gamma_2} & \mathbf{U}_{\Delta p}^{\Gamma_2} \end{bmatrix}. \quad (21)$$

The orthogonal basis for substructure 2 is constructed in the same way, to obtain

$$\mathbf{U}_{\Delta p, 2} = \begin{bmatrix} \mathbf{U}_{\Delta p}^{\Gamma_2} & \mathbf{0}^{\Gamma_2} \\ \mathbf{0}^{\Gamma_3} & \mathbf{U}_{\Delta p}^{\Gamma_3} \end{bmatrix}. \quad (22)$$

For some of the substructures, the grouping of $\mathbf{U}_{\Delta p}^{\Gamma}$ matrices is not necessary. For example, the bases used for substructures 3, 4 and 5 are simply given by

$$\mathbf{U}_{\Delta p, 3} = \mathbf{U}_{\Delta p}^{\Gamma_1}, \quad \mathbf{U}_{\Delta p, 4} = \mathbf{U}_{\Delta p}^{\Gamma_2}, \quad \text{and} \quad \mathbf{U}_{\Delta p, 5} = \mathbf{U}_{\Delta p}^{\Gamma_3} \quad (23)$$

Next, the orthogonal basis for each substructure is constructed using Eqs. (21), (22) and (23), and the interface DOFs (C) of the NX-PROMs generalized coor-

dinates are projected into the secondary generalized CC coordinates as shown in Eq. (12).

6.3. *L-shaped plate modeled with brick-type finite elements*

To demonstrate the proposed NX-PROM and LIR methodologies, an L-shaped structure modeled with brick-type elements (shown in Fig. 11) and containing thickness variations is investigated numerically. Figure (11) shows the pristine structure and the structure with thickness variations. The structure consists of eight substructures. Substructures 7 and 8 have three cases of thickness variations, as given in Table 2. The nominal thickness of the structure is 1 mm and the elemental thickness is 0.2 mm . The thickness variations applied are very large compared to the nominal elemental thickness considered. This causes the entries of the mass and stiffness matrices to vary nonlinearly. CB-CMS is applied for the 1st to the 6th substructure, and the NX-PROM approach is applied for the 7th and the 8th substructures.

Figure (12) shows the system-level forced responses of the nominal structure and the three cases of thickness variation. The dotted lines represent the vibration response of the nominal structure. The crosses and circles represent the responses of the structure with thickness variations predicted using NX-PROMs and full-order models, respectively. To reveal the enhanced performance of the NX-PROMs, the vibration response predicted by MC-PROMs is also shown by the stars in Fig. 12. For all three cases, the forced response predicted by the full-order models and the NX-PROMs show excellent matching. However, the forced responses predicted by MC-PROMs are not accurate compared to the full-order models. This is due to the fact that MC-PROMs cannot capture the volume variation of brick-type finite elements, which leads to poor predictions of the vibration

response. Note also that the thickness variations affect significantly the structure, as shown by the significant differences between the response of the nominal structure and the other responses.

The number of DOFs of the full-order model and the NX-PROMs are 18,300 and 3,502, respectively. The system-level DOFs of the NX-PROMs include 3,000 interface DOFs and 502 generalized internal DOFs. The number of generalized internal DOFs is small. However, the number of interface DOFs is large, and should be reduced. Thus, the LIR technique described in Section 4 was applied. Fig. 11 shows the interfaces which are reduced, where Γ_m indicates the m^{th} interface. Fig. 13 shows the forced responses for the nominal structure and the three cases of thickness variations. The dotted lines represent the response of the nominal structure. The crosses and circles indicate the responses of the structure with thickness variations predicted using NX-PROMs with full interface DOFs and full-order models, respectively. The squares represent the responses predicted using NX-PROMs with LIR. These latter models use only 533 interface DOFs, reduced by LIR from 2,498. The response predicted by NX-PROMs with LIR agree very well with the responses of the full-order model.

6.4. Results for a high mobility multipurpose wheeled vehicle model

In this section, NX-PROMs are used to predict the dynamic response of a realistic vehicle model. We consider the base frame of a high mobility multipurpose wheeled vehicle (HMMWV). The finite element model for the HMMWV is a conventional model used to examine its dynamic response [10, 11, 12, 13, 16]. Figure 14 shows the system-level and substructure-level finite element models of the HMMWV frame. The cross-bar structure is composed of substructures C_L and C_R , which are modeled with solid-type finite elements, as shown in Fig. 15.

The marked region in Fig. 15 indicates the nodes which move due to thickness variation. Table 3 indicates two cases of thickness variation for C_L and C_R . The thickness variations applied are much larger than those used in the L-shaped example. We chose these large variations to demonstrate that the proposed methods are very accurate even when the thickness variations are very large. Such large variations are encountered in practice especially when components are re-designed. The structural and the elemental thicknesses of the C_L and C_R substructures are 5 mm and 2.5 mm, respectively. NX-PROMs were created for the C_L and C_R substructures, and CB-CMS was applied to the remaining substructures. Next, forces and moments were applied to the engine cradle, and the resulting forced response were computed. Figure 16 shows the response of the HMMWV frame for cases 1 and 2. The measured point is shown in Fig. 14. The dotted line shows the forced response of the nominal HMMWV structure. The circles and crosses indicate the responses of the re-designed HMMWV frame predicted by full-order models and NX-PROMs, respectively. The stars show the responses predicted by MC-PROMs. Results obtained using the full-order models and the NX-PROMs show excellent agreement for both cases 1 and 2, but the results predicted by MC-PROMs do not agree well with the response obtained using the full-order models. Also, note that the re-design has important effects on the structure, as demonstrated by the significant difference between the responses of the nominal and the re-designed structures.

The full-order model of the HMMWV has 123,201 DOFs. The NX-PROMs have 2,683 DOFs, of which 1,473 are constraint DOFs and 1,210 are fixed-interface generalized DOFs. To reduce the number of constraint DOFs, LIR was applied. Figure 14 shows the interfaces of the substructures in the HMMWV frame. Ta-

ble 4 shows what are the interface DOFs for each substructure. Figure 17 shows the response of the HMMWV model predicted by NX-PROMs for cases 1 and 2 using different levels of reduction of the overall interface DOFs. Magnified plots near the resonant frequencies are included also. Note that the accuracy of the response predicted by LIR depends on the number of remaining interface DOFs. In these two cases, an acceptable accuracy is obtained when the remaining interface DOFs are not fewer than approximately 1,000.

7. Conclusions and Discussion

The key contributions of this paper are as follows. The proposed next-generation parametric reduced-order models (NX-PROMs) were developed by using a new parameterization technique to capture the element-level nonlinearity due to volume variations of finite elements of brick or other types. In addition, to establish a mathematically stable formulation for NX-PROMs, a new transformation matrix was developed using a novel interpolation of static constraint modes. Finally, a local-interface reduction (LIR) technique was proposed for further enhancing the computational efficiency of the NX-PROMs.

Novel, next-generation parametric reduced order models (NX-PROMs) for predicting the vibration response of complex structures have been presented. These models address two main drawbacks of MC-PROMs. The first is that the parameterization techniques used in MC-PROMs cannot capture the thickness variation of brick and other types of finite elements due to element-level nonlinearity of the stiffness matrix. The second drawback is that the transformation matrix for MC-PROMs is not numerically stable. Thus, a new parameterization technique was developed to capture the nonlinearity of the stiffness matrix, and a new trans-

formation matrix was proposed to make the NX-PROMs more stable numerically and more accurate compared to MC-PROMs.

To reduce the interface DOFs, a new method called local-interface reduction (LIR) was developed. NX-PROMs were developed for realistic substructural analysis. In such cases, the interface DOFs should be reduced before the system-level matrices are constructed. The LIR technique uses characteristic constraint modes computed *for each substructure* by using the constraint partition of the reduced mass and stiffness matrices constructed by CB-CMS or the NX-PROM approach. By using these characteristic constraint modes, orthogonal bases were defined to reduce the interface DOFs of each substructure. That is a key advantage of this reduction technique, and it is very useful for substructural analysis.

Similar to MC-PROMs, the novel NX-PROMs also provide smaller system matrices and shorter analysis and reanalysis time to predict the vibration response of complex structures. This means that NX-PROMs are especially useful for the repetitive analyses needed in optimization problems where geometric changes are applied in the design cycle for structures modeled with brick and other types of finite elements.

Acknowledgment

The authors gratefully acknowledge the financial support of the Automotive Research Center, a U.S. Army Center of Excellence for Modeling and Simulation of Ground Vehicles led by the University of Michigan.

Reference herein to any specific commercial company, product, process, or service by trade name, trademark, manufacturer, or otherwise, does not necessarily constitute or imply its endorsement, recommendation, or favoring by the

United States Government or the Department of the Army (DoA). The opinions of the authors expressed herein do not necessarily state or reflect those of the United States Government or the DoA, and shall not be used for advertising or product endorsement purposes.

UNCLASSIFIED: Dist A. Approved for public release.

References

- [1] W. C. Hurty, Dynamic analysis of structural systems using component modes, *AIAA Journal* 3 (4) (1965) 678–685.
- [2] R. R. Craig, Jr., M. C. C. Bampton, Coupling of substructures for dynamic analyses, *AIAA Journal* 6 (7) (1968) 1313–1319.
- [3] S. Rubin, Improved component-mode representation for structural dynamic analysis, *AIAA Journal* 13 (8) (1975) 995–1006.
- [4] R. M. Hintz, Analytical methods in component mode synthesis, *AIAA Journal* 13 (8) (1975) 1007–1016.
- [5] R. R. Craig, Jr., C.-J. Chang, Free-interface methods of substructure coupling for dynamic analysis, *AIAA Journal* 14 (11) (1976) 1633–1635.
- [6] M. P. Castanier, Y.-C. Tan, C. Pierre, Characteristic constraint modes for component mode synthesis, *AIAA Journal* 39 (6) (2001) 1182–1187.
- [7] W.-H. Shyu, J. Gu, G. M. Hulbert, Z.-D. Ma, On the use of multiple quasi-static mode compensation sets for component mode synthesis of complex structures, *Finite Elements in Analysis and Design* 35 (2) (2000) 119–140.

- [8] E. Balmès, Parametric families of reduced finite element modes: Theory and application., *Mechanical Systems and Signal Processing* 10 (4) (1996) 381–394.
- [9] D. L. E. Balmès, F. Ravary, Uncertainty propagation in modal analysis, in: *Proceedings of IMAC-XXII: A Conference and Exposition on Structural Dynamics*, Dearborn, MI, 2004, pp. IMAC–XXII–57.
- [10] G. Zhang, M. P. Castanier, C. Pierre, Integration of component-based and parametric reduced-order modeling methods for probabilistic vibration analysis and design., in: *Proceedings of the Sixth European Conference on Structural Dynamics*, Paris, France, 2005, pp. 993–998.
- [11] K. Park, G. Zhang, M. P. Castanier, C. Pierre, A component-based parametric reduced-order modeling technique and its application to probabilistic., in: *Proceedings of ASME International Mechanical Engineering Congress and Exposition*, Chicago, IL, USA, 2006, pp. IMECE2006–15069.
- [12] K. Park, Component-based vibration modeling methods for fast reanalyses and design of complex structures, Ph.D. thesis, University of Michigan (2008).
- [13] S. K. Hong, B. I. Epureanu, M. P. Castanier, D. J. Gorsich, Parametric reduced-order models for predicting the vibration response of complex structures with component damage and uncertainties., *Journal of Sound and Vibration* 330 (2011) 1091–1110.
- [14] O. C. Zienkiewicz, R. L. Taylor, *The Finite Element Method*, Butterworth Heinemann, 1967.

- [15] T. J. R. Hughes, *The Finite Element Method Linear Static and Dynamic Finite Element Analysis*, Dover, 2000.
- [16] S. K. Hong, B. I. Epureanu, M. P. Castanier, Novel sensor placement for damage identification in a cracked complex structure with structural variability, *Journal of Intelligent Material Systems and Structures*-doi:10.1177/00000000000411217.

List of Tables

1	10 lowest natural frequencies for exact and parametrized matrices with volume variations	33
2	Thickness variations in substructures 7 and 8 of the L-shaped plate	34
3	Thickness variations in substructures C_L and C_R of the HMMWV frame	35
4	Interfaces between substructures in the HMMWV model	36

Table 1: 10 lowest natural frequencies for exact and parametrized matrices with volume variations

Mode	Exact	Approximated
1	4278.24	4278.24
2	9024.39	9011.52
3	9068.45	9053.21
4	14323.12	14323.11
5	24952.70	24952.34
6	25024.01	25023.94
7	27463.11	27460.10
8	27656.15	27654.70
9	36098.49	36098.51
10	41275.58	41262.95

Table 2: Thickness variations in substructures 7 and 8 of the L-shaped plate

Substructure	Thickness, case 1	Thickness, case 2	Thickness, case 3
7	1.00 mm \rightarrow 1.22 mm	1.00 mm \rightarrow 1.42 mm	1.00 mm \rightarrow 1.81 mm
8	1.00 mm \rightarrow 1.22 mm	1.00 mm \rightarrow 1.42 mm	1.00 mm \rightarrow 1.81 mm

Table 3: Thickness variations in substructures C_L and C_R of the HMMWV frame

Substructure	Thickness, case 1	Thickness, case 2
C_L	5 mm \rightarrow 20 mm	5 mm \rightarrow 32 mm
C_R	5 mm \rightarrow 20 mm	5 mm \rightarrow 32 mm

Table 4: Interfaces between substructures in the HMMWV model

Substructure Interface	1	2	3	4	5	6	7	8	9	10
Γ_1	O	O								
Γ_2	O								O	
Γ_3	O							O		
Γ_4		O					O			
Γ_5			O						O	
Γ_6			O				O			
Γ_7				O				O		
Γ_8				O		O				
Γ_9					O			O		
Γ_{10}					O	O				
Γ_{11}						O	O			
Γ_{12}								O	O	
Γ_{13}									O	O
Γ_{14}							O			O

List of Figures

1	Sample 8-node brick element with global and local coordinates . . .	39
2	The case where the value of parameter p is between $p_0+l\delta p$ and $p_0+(l+1)\delta p$ for some l value between 0 and 3	40
3	Simple plate structure modeled with shell-type elements	41
4	The 32 nd diagonal entries of the exact and the parametrized mass and stiffness matrices obtained by using a classic cubic interpolation for shell-type elements	42
5	Simple plate structure modeled with brick-type elements	43
6	The 645 th diagonal entry of the exact and the parametrized stiffness matrices obtained by using a classic cubic interpolation (left) and an classic fourth order interpolation (right) for brick-type elements	44
7	Forced responses calculated for $\Delta p = 0.37 \text{ mm}$ using the exact and parametrized mass and stiffness matrices obtained based on a fourth-order interpolation for brick-type elements	45
8	The 645 th diagonal entry of the exact and the parametrized stiffness matrices obtained by using the new interpolation for brick-type elements	46
9	Forced response calculated for $\Delta p = 0.37 \text{ mm}$ using the exact and the parametrized mass and stiffness matrices obtained based on the new interpolation for brick-type elements	47
10	A simple structure used to demonstrate the local-interface reduction	48

11	An L-shaped plate shown without thickness variation (left) and with thickness variation (right); interfaces between components are denoted by Γ_i	49
12	Forced response predictions of the L-shaped plate for the nominal structure and for cases 1, 2 and 3 computed using full-order models, MC-PROMs and the novel NX-PROMs	50
13	Forced response predictions of the L-shaped plate for the nominal structure and for cases 1, 2 and 3 computed using full-order models, NX-PROM, and NX-PROM with LIR	51
14	System-level and substructure-level finite element models of the frame of a high mobility multipurpose wheeled vehicle	52
15	Nominal and re-designed cross-bar composed of C_L and C_R	53
16	Forced response predictions for the HMMWV frame for the nominal structure and for cases 1 (top) and 2 (bottom)	54
17	Forced response predictions for the HMMWV frame obtained using NX-PROMs with LIR for different levels of reduction; the total number of DOFs obtained for each model using LIR are indicated for case 1 (left) and 2 (right)	55

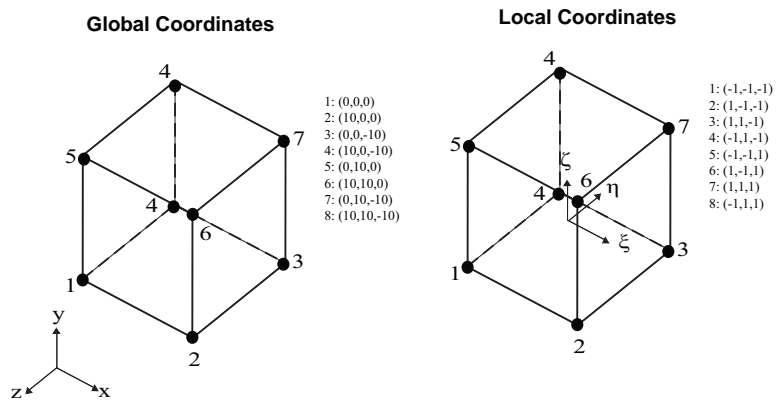


Figure 1: Sample 8-node brick element with global and local coordinates

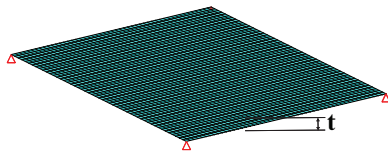


Figure 3: Simple plate structure modeled with shell-type elements

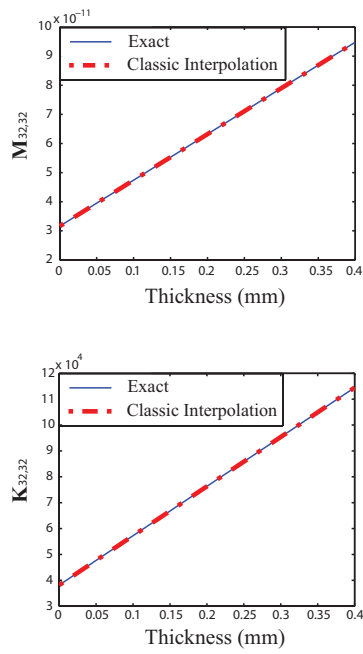


Figure 4: The 32nd diagonal entries of the exact and the parametrized mass and stiffness matrices obtained by using a classic cubic interpolation for shell-type elements

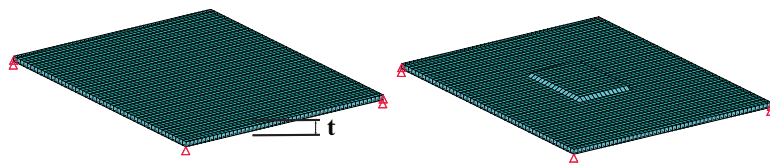


Figure 5: Simple plate structure modeled with brick-type elements

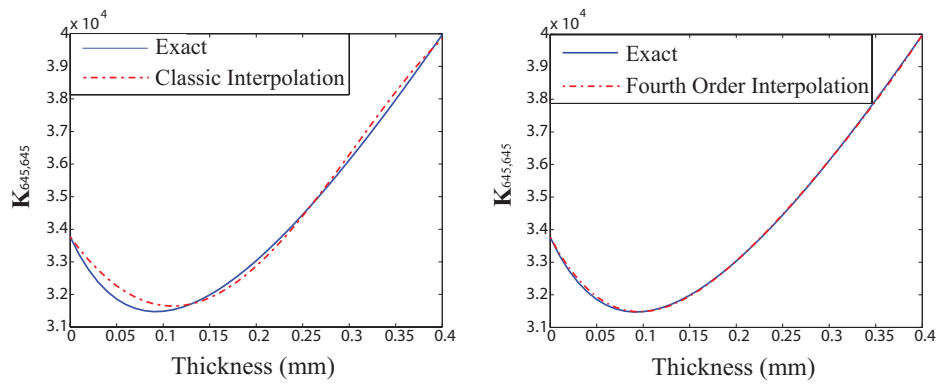


Figure 6: The 645th diagonal entry of the exact and the parametrized stiffness matrices obtained by using a classic cubic interpolation (left) and an classic fourth order interpolation (right) for brick-type elements

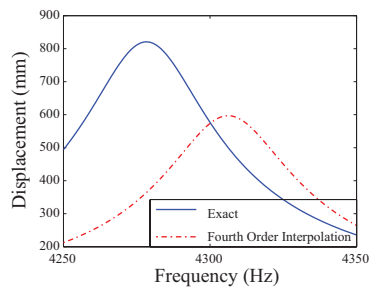


Figure 7: Forced responses calculated for $\Delta p = 0.37 \text{ mm}$ using the exact and parametrized mass and stiffness matrices obtained based on a fourth-order interpolation for brick-type elements

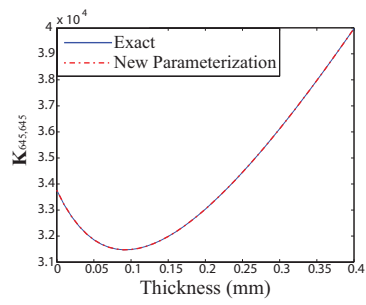


Figure 8: The 645th diagonal entry of the exact and the parametrized stiffness matrices obtained by using the new interpolation for brick-type elements

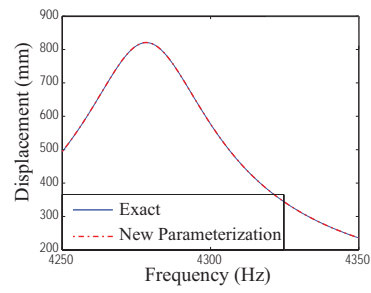


Figure 9: Forced response calculated for $\Delta p = 0.37 \text{ mm}$ using the exact and the parametrized mass and stiffness matrices obtained based on the new interpolation for brick-type elements

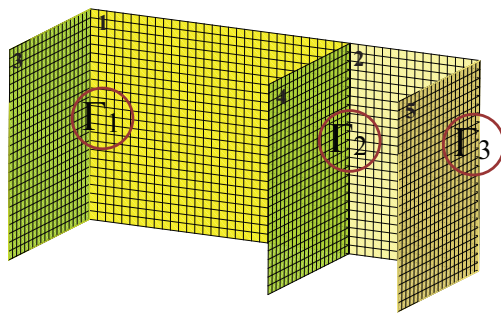


Figure 10: A simple structure used to demonstrate the local-interface reduction

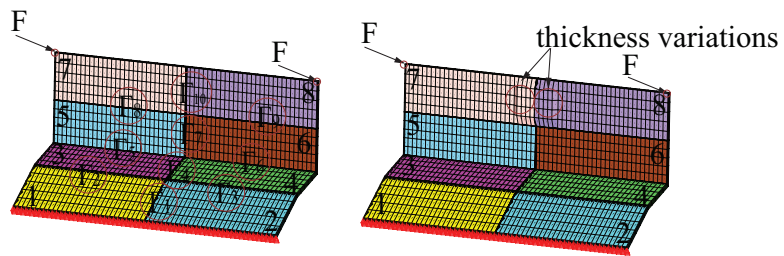


Figure 11: An L-shaped plate shown without thickness variation (left) and with thickness variation (right); interfaces between components are denoted by Γ_i

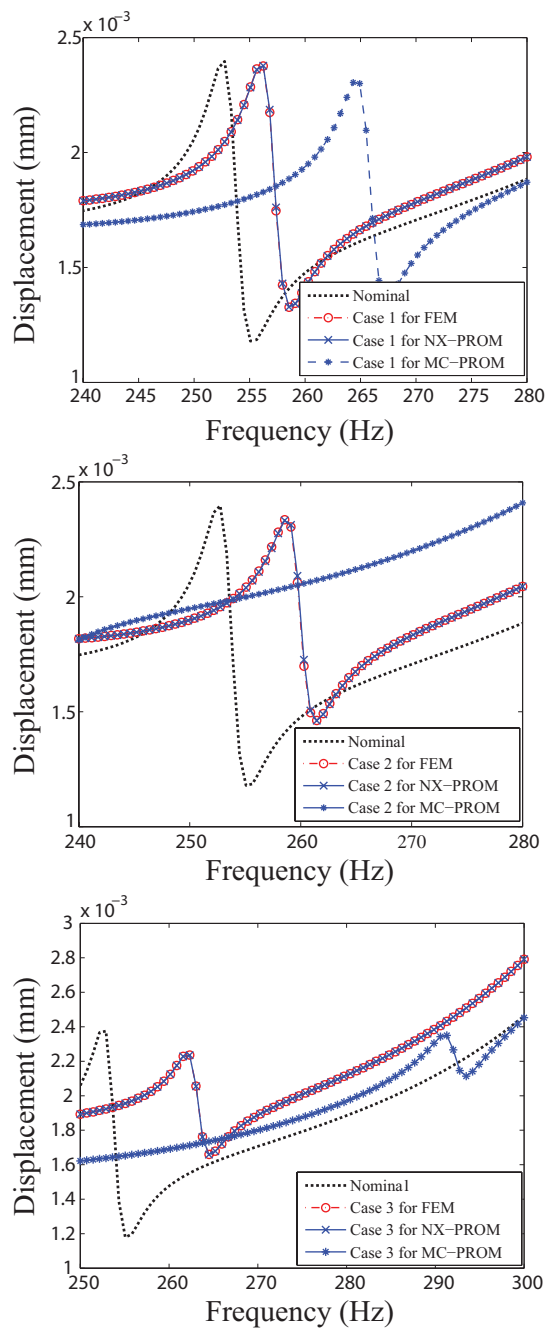


Figure 12: Forced response predictions of the L-shaped plate for the nominal structure and for cases 1, 2 and 3 computed using full-order models, MC-PROMs and the novel NX-PROMs

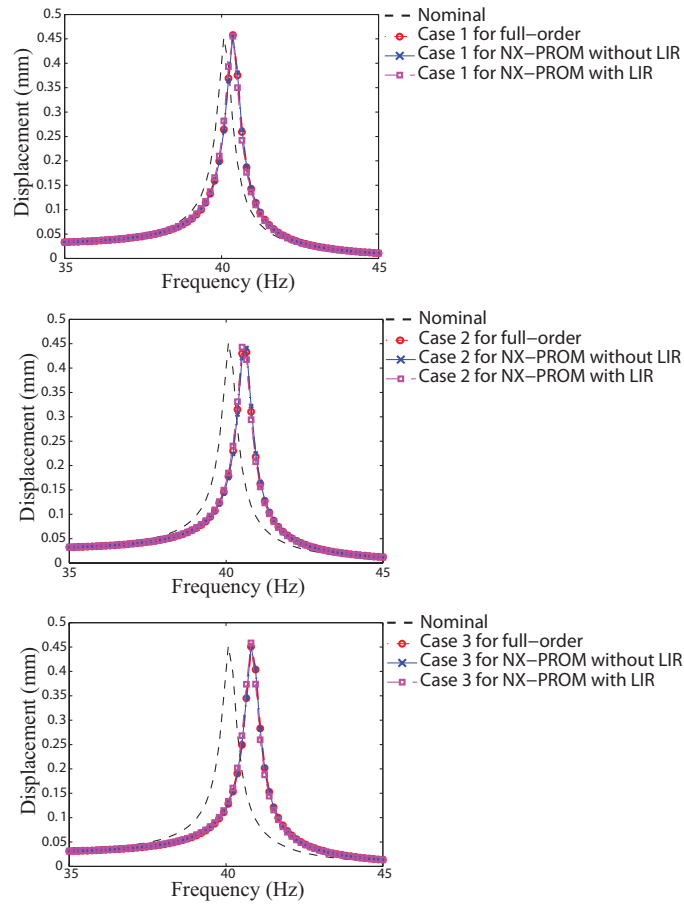


Figure 13: Forced response predictions of the L-shaped plate for the nominal structure and for cases 1, 2 and 3 computed using full-order models, NX-PROM, and NX-PROM with LIR

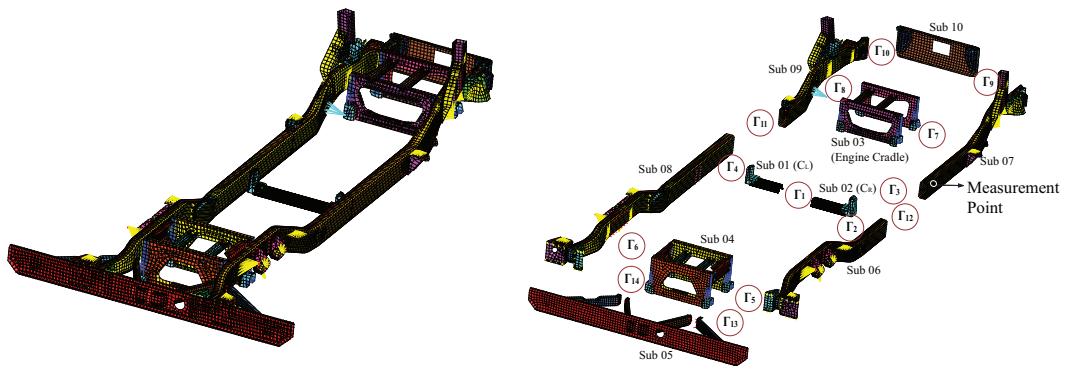


Figure 14: System-level and substructure-level finite element models of the frame of a high mobility multipurpose wheeled vehicle

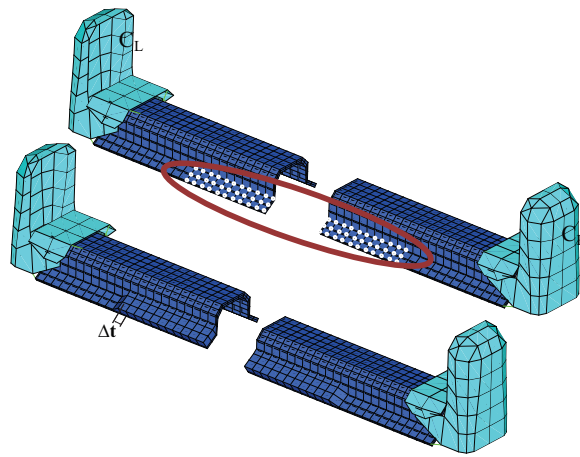


Figure 15: Nominal and re-designed cross-bar composed of C_L and C_R

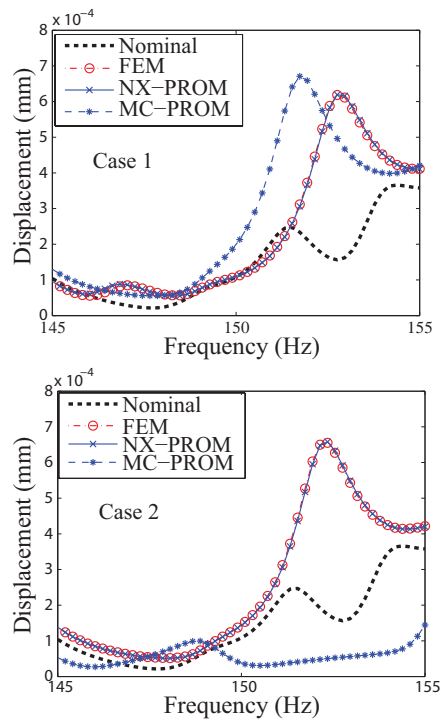


Figure 16: Forced response predictions for the HMMWV frame for the nominal structure and for cases 1 (top) and 2 (bottom)

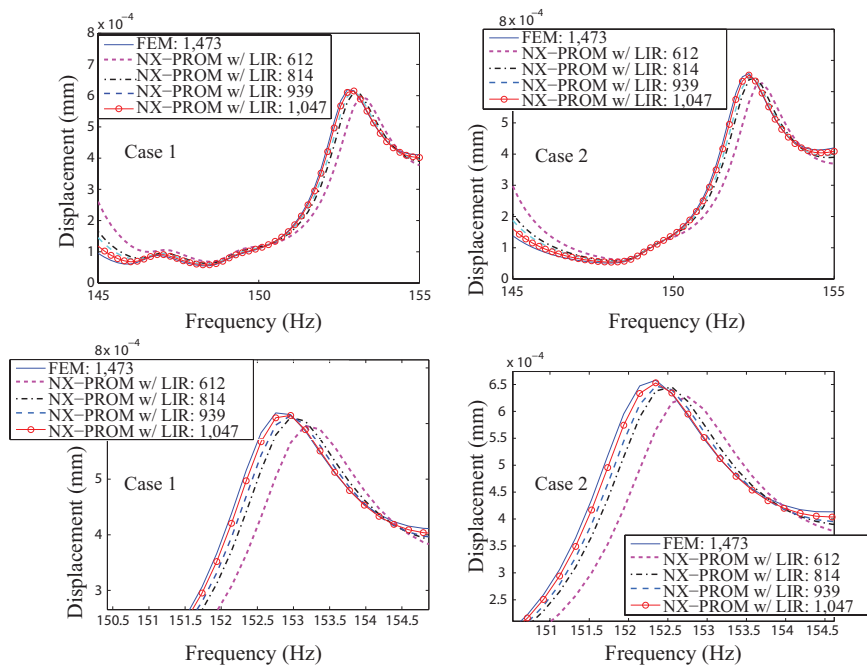


Figure 17: Forced response predictions for the HMMWV frame obtained using NX-PROMs with LIR for different levels of reduction; the total number of DOFs obtained for each model using LIR are indicated for case 1 (left) and 2 (right)